AIAA 2001-3441

DEVELOPMENT OF FLOW AND HEAT TRANSFER MODELS FOR THE CARBON FIBER ROPE IN NOZZLE JOINTS OF THE SPACE SHUTTLE REUSABLE SOLID ROCKET MOTOR

Q. Wang, M.E. Ewing, E.C. Mathias, J. Heman, C. Smith
ATK Thiokol Propulsion Corp.
P.O. Box 707, M/S 252
Brigham City, UT 84302

37th AIAA/ASME/SAE/ASEE
Joint Propulsion Conference and Exhibit
July 8-11, 2001
Salt Lake City, Utah

Development of Flow and Heat Transfer Models for the Carbon Fiber Rope in Nozzle Joints of the Space Shuttle Reusable Solid Rocket Motor

Qunzhen Wang[*], Mark Ewing[+], Ed Mathias[+], Cory Smith[§] and Joe Heman[+]
ATK Thiokol Propulsion Company, Brigham City, UT

Methodologies have been developed for modeling both gas dynamics and heat transfer inside the carbon fiber rope (CFR) for applications in the space shuttle reusable solid rocket motor joints. Specifically, the CFR is modeled using an equivalent rectangular duct with a cross-section area, friction factor and heat transfer coefficient such that this duct has the same amount of mass flow rate, pressure drop, and heat transfer rate as the CFR. An equation for the friction factor is derived based on the Darcy-Forschheimer law and the heat transfer coefficient is obtained from pipe flow correlations. The pressure, temperature and velocity of the gas inside the CFR are calculated using the one-dimensional Navier-Stokes equations. Various subscale tests, both cold flow and hot flow, have been carried out to validate and refine this CFR model. In particular, the following three types of testing were used: (1) cold flow in a RSRM nozzle-to-case joint geometry, (2) cold flow in a RSRM nozzle joint No. 2 geometry, and (3) hot flow in a RSRM nozzle joint environment simulator. The predicted pressure and temperature history are compared with experimental measurements. The effects of various input parameters for the model are discussed in detail.

INTRODUCTION

The carbon fiber rope (CFR), which was originally developed at NASA Glenn Research Center to meet the requirements of advanced hypersonic engines,[1,2] is being considered as a replacement for the thermal barriers currently used to protect O-rings in the joints of the space shuttle reusable solid rocket motor (RSRM), specifically, the nozzle-to-case joint and nozzle joint No. 2. The CFR currently under consideration readily conforms to various RSRM joint assembly conditions, and has the ability to cool combustion gases, filter slag and particulates, and diffuse impinging gas jets.[3,4,5,6] Steinetz and Dunlap[7] have studied the feasibility of using a CFR as a thermal barrier to hot combustion gases inside RSRM joints and found that a CFR could withstand 2500°F combustion gases on the upstream side with very little temperature rise on the downstream side. Foote[8] also describes the similar use of a CFR, for the purpose of slag filtering, in the field joints of the Titan IV solid rocket motor.

The main objective of this paper is to develop both flow and heat transfer models for the CFR in RSRM joints within the framework of SFLOW[9]. SFLOW is a thermal-flow code recently developed to model the gas dynamics and heat transfer inside RSRM joints by combining SINDA/G[10], a commercial thermal analyzer, and SHARP[11,12,13], a general purpose computational fluid dynamics (CFD) code. The pressure, temperature and velocity of the gas in the flow paths are calculated in SHARP by solving the one-dimensional Navier-Stokes equations in a time-accurate manner while the heat conduction in the solid is modeled by SINDA/G. SFLOW is much more accurate than ORING2 and other similar codes[14,15] where empirical correlations are used to predict the mass flow rate and other flow properties by assuming the flow is adiabatic and quasi-steady. On the other hand, a SFLOW prediction takes much less CPU time than a transient 3D CFD calculation because of the 1D flow assumption and the larger time step in the solid region,

The problem of modeling flow and heat transfer in this application is complicated by highly transient and compressible flow conditions. Very little relating to the topic can be found in the open literature. Some work has been reported on related flow modeling by the NASA Glenn Research Center, which was aimed at the prediction of leakage through the porous CFR "seal." Specifically, Mutharasan *et al.* [16,17] proposed a mathematical model for leakage flow through the braided rope which enables prediction of gas leakage rate as a function of fiber diameter, fiber packing density, gas properties, and the pressure drop across the rope. This model was later modified by Cai *et al.* [18,19] to take into account the effect of lateral preload and

---

Published by the American Institute of Aeronautics and Astronautics, Inc., with permission.

[*] Sr. Principal Engineer, Gas Dynamics, AIAA member

[+] Sr. Principal Engineer, Heat Transfer, AIAA member

[§] Senior Engineer, Heat Transfer

engine pressures.

While these models could be used to predict mass flow rates through the CFR if the pressure drop across the rope is known, they do not address the heat transfer between gas and solid inside the CFR. The heat transfer is an important part of the present study because gas temperature downstream of the CFR and whether this temperature is high enough to cause hardware problems are the major concerns in RSRM applications. Moreover, as shown later in this paper, the heat transfer from the hot combustion gas to the solid surfaces strongly affects the mass flow rate. Furthermore, the influence of gland geometries may result in flow resistances that differ from those in the NASA-Glenn studies.

Methodologies are developed in this paper for modeling both the gas dynamics inside CFR and the heat transfer from hot combustion gases to solid fibers. In particular, the CFR is modeled using an equivalent rectangular duct with a cross-section area, friction factor and heat transfer coefficient such that the mass flow rate, pressure drop, and heat transfer rate are the same as those in the CFR. The pressure, temperature and velocity of the gas inside this duct are calculated using the one-dimensional Navier-Stokes equations. An equation for the friction factor is derived based on the Darcy-Forschheimer law and the heat transfer coefficient is obtained from pipe flow correlations. Note that this model is similar to those of Emanuel and Jones[20], Beavers and Sparrow[21], as well as the so-called capillary models[22] in that they all involve applications of the Navier-Stokes equations to flows in small cross-section area ducts. However, there are important differences. For example, while the current model considers the flow to be transient with heat transfer between gas and solid, all other models assume the flow is steady and adiabatic. Note also that, while most of the porous media literature assumes thermal equilibrium conditions (i.e., no temperature difference between gas and solid inside the porous material) [23], the CFR model developed in this paper is a non-equilibrium heat transfer model since a large temperature difference could occur between the fluid phase and solid phase in the application of CFR to the space shuttle RSRM joints due to the highly transient nature of the flow process.

Various subscale tests, both cold flow and hot flow, have been carried out to validate and refine the current CFR model. In particular, the following three types of testing were used: (1) cold flow in a RSRM nozzle-to-case joint geometry[5], (2) cold flow in a RSRM joint 2 geometry[6], and (3) hot flow in a RSRM nozzle joint environment simulator (JES)[6,24]. Parameters needed in the CFR models such as permeability are derived from these tests by matching predicted results with measured data. The predicted pressure and temperature history at various locations are compared with experimental measurements.

This paper is organized as follows. The governing equations and numerical methods used in SFLOW are summarized in the next section followed by details of the CFR model. The predicted pressure and temperature from SFLOW using this model as well as the effects of various input parameters are presented next. Finally, the conclusions are summarized and future work is discussed.

NUMERICAL METHODS

In SFLOW, the gas can be either in a flow path or a volume (i.e., cavity), which are treated very differently. The gas in a volume is assumed to be in an equilibrium state with no velocity and uniform pressure and temperature (i.e., pressure and temperature are functions of time only) whereas the pressure, temperature and velocity in a path are functions of both time and location. A path has to be connected with a volume at one end; the other end can be connected to a volume or a solid wall, which could be either adiabatic or conducting heat away to the solid region. Details of how the flow fields in both paths and volumes are solved as well as how the friction factor and heat transfer coefficient are obtained in SFLOW are discussed in this section.

Pressure, Temperature and Velocity in Paths

The transient compressible flow in a path is modeled using SHARP[11,12,13], which is a general-purpose CFD code. While SHARP can solve 1D, 2D as well as 3D problems, all results shown in this paper assume one-dimensional flow in paths to save CPU time and memory. In 1D, SHARP solves the Navier-Stokes equation as

$$\frac{\partial Q}{\partial t} + \frac{\partial (E_i - E_v)}{\partial x} = S \qquad (1)$$

where the unknowns are

$$Q = A \begin{bmatrix} \rho \\ \rho u \\ e \end{bmatrix} \qquad (2)$$

In equation (2), A is the cross-section area, which could be a function of both space x and time t, and ρ and u

are the gas density and velocity, respectively. The total energy is

$$e = \rho\left(c_v T + \frac{1}{2}u^2\right) \quad \textbf{(3)}$$

where T is the gas temperature and c_v is the specific heat at constant volume. The inviscid flux term is given by

$$E_i = A\begin{bmatrix} \rho u \\ \rho u^2 + p \\ (e+p)u \end{bmatrix} \quad \textbf{(4)}$$

while the viscous term is

$$E_v = A\begin{bmatrix} 0 \\ \tau_{11} \\ u\tau_{11} + q_1 \end{bmatrix} \quad \textbf{(5)}$$

where τ_{11} and q_1 are the stress and heat flux, respectively. The source term in equation (1) is

$$S = \begin{bmatrix} \dfrac{\dot{m}_e A}{V} \\ -\dfrac{fA\rho u\,|\,u\,|}{2D_h} - \dfrac{1}{2}\dfrac{\partial(\beta A\rho u\,|\,u\,|)}{\partial x} \\ -\dot{q}\dfrac{A}{V} - \dfrac{fA\rho|u|^3}{2D_h} - \dfrac{1}{2}\dfrac{\partial(\beta A\rho u^3)}{\partial x} \end{bmatrix} \quad \textbf{(6)}$$

where $\dot{m}_e$ is the mass addition rate due to path erosion, V is the volume of the flow cell, f is the Darcy friction factor, D_h is the hydraulic diameter of the path, β is the minor loss coefficient and $\dot{q}$ is the heat transfer rate from gas to solid walls. The boundary conditions for the path flowfield are obtained from the pressure and temperature of the volumes connected to this path.

Note that the friction term is explicitly accounted for in equation (6) because the velocity gradient $\partial u/\partial y$ does not exist in 1D. Similarly, the heat transfer term is added in equation (6) due to the fact that the thermal boundary layer is not simulated in SFLOW. The mass addition terms are also added since the erosion or decomposition of the walls will generate this effect. Finally, minor loss terms such as those due to sudden expansion or contraction and turns or bends in the flow path are added in equation (6).

The friction factor in equation (6) is obtained from the empirical correlation of Idelchik[25] based on both the shape of the path (i.e., circular, rectangular, or triangular) and whether the flow is laminar, turbulent, or in transition. The gas flow is divided into laminar, turbulent, and transitional regimes depending on the cutoff Reynolds numbers defined as

$$\mathrm{Re}_a = 754\exp(0.0065 D_h/\varepsilon) \quad \textbf{(7)}$$

$$\mathrm{Re}_b = 1160\left(\frac{D_h}{\varepsilon}\right)^{-0.11} \quad \textbf{(8)}$$

$$\mathrm{Re}_c = 2090\left(\frac{D_h}{\varepsilon}\right)^{-0.0635} \quad \textbf{(9)}$$

where ε is the roughness of the flow path. The flow is laminar if the Reynolds number is below Re_a, turbulent if the Reynolds number is above Re_c, and in transitional regime if the Reynolds number is between Re_a and Re_c. If there are two transitional zones, Re_b is used to determine which of the two zones the flow is in.

The friction factor in a circular flow path is determined based on the flow Reynolds number $\mathrm{Re}=\rho u D_h/\mu$, where μ is the molecular viscosity, as:

- for $\mathrm{Re} < \mathrm{Re}_a$

$$f = \frac{64}{\mathrm{Re}} \quad \textbf{(10)}$$

- for $\mathrm{Re}_a \le \mathrm{Re} < \mathrm{Re}_b$

$$f = 4.4\,\mathrm{Re}^{-0.595}\exp\left(\frac{-0.00275\varepsilon}{D_h}\right) \quad \textbf{(11)}$$

- for $\mathrm{Re}_b \le \mathrm{Re} < \mathrm{Re}_c$

$$f = \left(0.145\left(\frac{\varepsilon}{D_h}\right)^{0.244} - Val\right)\exp\left(-0.0017^2(\mathrm{Re}_c - \mathrm{Re})^2\right) + Val \quad \textbf{(12)}$$

$$Val = 0.758 - 0.0109\left(\frac{\varepsilon}{D_h}\right)^{-0.286} \quad \textbf{(13)}$$

- for $\mathrm{Re} \ge \mathrm{Re}_c$

$$f^{-1/2} = -2\log\left(\frac{\varepsilon}{3.7D_h} + \frac{2.51}{\mathrm{Re}\sqrt{f}}\right) \quad \textbf{(14)}$$

- for $\mathrm{Re}_a \le \mathrm{Re} < \mathrm{Re}_c$ and $\mathrm{Re}_b \le \mathrm{Re}_a$ there is only one transitional zone

$$f = \left(7.244\,\mathrm{Re}^{-0.643} - 0.32\right) \quad \textbf{(15)}$$
$$\times\exp\left(-0.0017^2(\mathrm{Re}_c - \mathrm{Re})^2\right) + 0.032$$

If the flow path is rectangular, the friction factor in the above equations is multiplied by

$$F_{lam} = 1.5 - 1.9r + 1.96r^2 - 0.71r^3 \qquad (16)$$

for laminar flow and

$$F_{turb} = 1.1 - 0.2r + 0.2r^2 - 0.078r^3 \qquad (17)$$

for turbulent flow. The ratio of width and height is defined as

$$r = \min\left[16, \frac{\max(a,b)}{\min(a,b)}\right] \qquad (18)$$

with a and b being the width and height of the flow path.

Pressure and Temperature in Volumes

Once the flowfield in the path is solved by SHARP, the pressure and temperature in the volumes can be obtained from mass conservation

$$\frac{\partial m}{\partial t} = \dot{m}_e + \sum \dot{m} \qquad (19)$$

and energy conservation

$$\frac{\partial}{\partial t}\left(mc_v T\right) = \sum \dot{m}_p \left(c_p T_p + \frac{1}{2} u_p^{\,2}\right) - \dot{q} \qquad (20)$$

where the summation is for all paths which connect to this volume, $\dot{m}_p$, T_p and u_p are the mass flow rate, temperature and velocity at the end of the path, $\dot{m}_e$ is the rate of mass addition to the gas due to surface erosion, $\dot{q}$ is the heat transfer rate from the gas to the solid boundary which includes the convective heat transfer as well as the heat transfer due to erosion. In addition to equations (19) and (20), the ideal gas law

$$pV = mRT \qquad (21)$$

where V is the volume of the cavity, was used to solve the pressure p, temperature T, and mass m of the volume.

Heat Transfer in Paths

The heat transfer coefficient in flow paths can be obtained from the Nusselt number as

$$h = N_u \frac{k}{D_h} \qquad (22)$$

where k is the thermal conductivity. According to Idelchik[25], the Nusselt number depends on both the cross-section shape of the path and the flow regime. If the flow is laminar and the path is circular

$$N_u = 4.36 \qquad (23)$$

while for rectangular paths

$$N_u = 1.18135 + 2.30595r^{0.403245} \qquad (24)$$

where the ratio r is defined in equation (18). For turbulent flow, the Nusselt number is calculated using the following empirical correlation

$$N_u = \frac{f \,\mathrm{Pr}\,\mathrm{Re}}{\max\left(\mathrm{Pr}^{2/3}, \left(1.07 - 12.7\sqrt{f/8}\left(\mathrm{Pr}^{2/3} - 1\right)\right)\right)} \left(\frac{\mu_B}{\mu_w}\right)^{0.14} \qquad (25)$$

where μ_B and μ_w are the viscosity evaluated at the average gas temperature and wall temperature, respectively. In the transitional regime, a linear interpolation between the laminar and turbulent Nusselt number is applied.

SFLOW can also model the jet impingement heat transfer (see reference 9 for details), which usually has a much larger heat transfer coefficient than that from the above equations.

Heat Transfer in Volumes

The heat transfer from the gas in a volume to the solid boundary can be modeled in the following four different ways: (1) using the impingement jet heat transfer correlation; (2) using the heat transfer coefficient in the paths connected to this volume; (3) using a conduction length as $h=k/l$; and (4) using a user-specified heat transfer coefficient. The user of SFLOW specifies which of these methods should be applied to calculate heat transfer coefficient for all the gas-solid interfaces in all volumes.

CFR MODELING

In this paper, the CFR is modeled using an equivalent rectangular duct with cross-section area A, friction factor f and heat transfer coefficient h. The pressure, temperature and velocity of the gas inside this duct are then calculated using the Navier-Stokes equations (1) through (6). The idea is to model the CFR with a duct that has the same amount of mass flow rate, pressure drop, and heat transfer rate.

Gas Dynamics

The Darcy-Forschheimer's law for transient compressible flow is given by[21,23]

$$\rho\frac{\partial u}{\partial t} + \rho u \frac{\partial u}{\partial x} + \frac{\partial p}{\partial x} + \frac{\mu}{\mathrm{K}} v + b\frac{\rho v^2}{2} = 0 \qquad (26)$$

where the permeability and velocity based on the Darcy area A_D (usually frontal area) are denoted by K and v, respectively, while ρ is the fluid density and u is the local velocity based on the pore area A. The Forschheimer constant is usually written in terms of the permeability as

$$b = c/\sqrt{K} \qquad (27)$$

where c is a non-dimensional empirical constant. For one-dimensional compressible flows in a constant area duct, the momentum conservation law is

$$\rho\frac{\partial u}{\partial t} + \rho u\frac{\partial u}{\partial x} + \frac{\partial p}{\partial x} + \frac{\rho u^2}{2}\frac{f}{D_h} = 0 \qquad (28)$$

Combining equations (26) and (28) yields

$$\frac{\rho u^2}{2}\frac{f}{D_h} = \frac{\mu}{K}v + b\frac{\rho v^2}{2} \qquad (29)$$

Therefore, the friction factor can be calculated from the permeability as

$$f = \frac{2\mu D_h}{K}\frac{v}{\rho u^2} + D_h\frac{c}{\sqrt{K}}\frac{v^2}{u^2} \qquad (30)$$

The mass flow rate in the Darcy configuration with a cross-section area of A_D is assumed to be the same as that in the SFLOW configuration with a cross-section area of A, i.e.,

$$\rho A u = \rho A_D v = \dot{m} \qquad (31)$$

Substituting equation (31) into equation (30) yields

$$f = \frac{2\mu D_h}{\rho u K}\phi + \frac{c}{\sqrt{K}}D_h\phi^2 \qquad (32)$$

where the porosity is defined as

$$\phi = \frac{A}{A_D} \qquad (33)$$

The above derivations indicate that, if equation (32) is used to calculate the friction factor in SFLOW, the mass flow rate through the CFR and pressure drop across the CFR will be the same as those corresponding to that through a porous media with a Darcy area of A_D, permeability of K and Forschheimer constant of c. The input parameters for this CFR model are Darcy area A_D, hydraulic diameter D_h, permeability K, Forschheimer constant c, and porosity ϕ. All of these parameters are assumed to be constant (i.e., independent of both location and time) in all results shown in this paper. The cross-section area A is obtained from the Darcy area and porosity using equation(33).

If the Forschheimer constant in equation (32)is assumed to be zero, the friction factor can be written as

$$f = \frac{2\mu D_h}{\rho u K}\phi \qquad (34)$$

Considering equation (31), the above equation becomes

$$f = \frac{2\mu D_h A_D}{\dot{m}K}\phi^2 \qquad (35)$$

Equation (35) shows that, as expected, the friction factor is inversely proportional to the permeability. A large permeability corresponds to small friction factor and small permeability to large friction factor for fixed porosity and Darcy area if the Forschheimer term is neglected. Equation (32) indicates that the friction factor is linearly proportional to the hydraulic diameter and the Forschheimer constant. However, the hydraulic diameter has no effect on the flow field because, as shown in equation (28), what appears in the governing equation is f/D_h, which is independent of the hydraulic diameter.

Equation (35) also shows that the friction factor is proportional to the square of porosity while equation(33) indicates that area is linearly proportional to porosity. Therefore, increasing the porosity by a factor of 10 increases the friction factor by a factor of 100 and cross-section area by 10 for fixed permeability and Darcy area. Note that there is no constraint on the porosity in the above derivations and, thus, one can choose an arbitrary porosity for the CFR. That is, for a fixed permeability and Darcy area, one can use a small porosity (i.e., small cross-section area) with a small friction factor or a large porosity (i.e., large cross-section area) with a large assumed friction factor to keep the same mass flow rate and pressure drop across the CFR. Therefore, the porosity has no effect on the solution of gas flow through a CFR. This is not true, however, when the friction factor is large enough such that the flow across the CFR is choked, where the mass flow rate does not change when the friction factor is increased further. Instead, the mass flow rate will be a function of cross-section area only and increasing the porosity will increase the mass flow rate even though the friction factor is also increased. Furthermore, as discussed later in this paper, when there is heat transfer between gas and solid, the porosity affects the amount of gas inside the CFR and, thus, affects the mass flow rate. Note also that, even for unchoked adiabatic flow, porosity may have some effect on the flow field due to the transient and convective terms in equation (26). These two terms are usually neglected in porous media studies and, in that case, the porosity has no effect on the pressure, temperature and velocity of the gas inside the CFR if the flow is adiabatic and unchoked.

Neglecting the transient term, convective term as well as the Forschheimer term in equation (26), the mass flow rate can be written as

$$\dot{m} = \frac{\rho \Delta p K A_D}{\mu L} \qquad (36)$$

where L is the length of the CFR and Δp is the pressure drop across the CFR. Therefore, the mass flow rate does not change as long as KA_D is constant because ρ, Δp, μ, and L are fixed for a particular problem. That is, if the Darcy area is reduced by a factor of 10, the permeability should be increased by a factor of 10 in order to keep the same mass flow rate.

Heat Transfer

Most of the porous media literature assumes thermal equilibrium conditions (i.e., no temperature difference between gas and solid inside the porous material).[23] However, as discussed in Bellettre *et al.*[26] and Kaviany[22], a large temperature difference could occur between the fluid phase and solid phase under certain conditions. This is especially true in the application of CFR to the space shuttle RSRM joints due to the highly transient nature of the flow process. Therefore, a non-equilibrium heat transfer model of the CFR has been developed where the convective heat transfer coefficient between the gas inside the CFR and the solid is modeled using equations (22) to (25). In addition to Darcy area, hydraulic diameter, permeability, Forschheimer constant, and porosity, the surface area has to be specified for each gas-solid interface to obtain the heat transfer rate. In SFLOW, the total surface area for all CFR surfaces is an input parameter and the area of each CFR surface is obtained by assuming it is proportional to the volume of the corresponding CFR solid node.

The surface area has to be specified properly. A very large surface area will make the code unstable since the calculated heat transfer may be larger than the amount of energy available in the gas. On the other hand, a very small surface area does not provide enough heat transfer and, thus, the gas temperature after the rope would be too high. The convective heat transfer rate from the gas inside the CFR to the solid surfaces is limited by the heat transfer rate which causes the temperature of the solid surfaces to equilibrate with the gas temperature during one time step. Specifically, to make sure the code is stable, the heat transfer rate is limited by

$$\dot{q} = hA_s(T_g - T_w) \le \frac{\rho A \Delta x c_p (T_g - T_w)}{\Delta t} \quad \textbf{(37)}$$

where Δx, Δt, T_g and T_w are the length of the flow cell, time step, gas temperature, and wall temperature, respectively. Note that, if either surface area or time step is too large, this limiter kicks in and the results would depend on the time step. In all SFLOW predictions shown in this paper, the surface area and time step are chosen to be small enough such that equation (37) is always satisfied.

Considering equation (22), the heat transfer rate can be written as

$$\dot{q} = kN_u(T_g - T_w)\frac{A_s}{D_h} \quad \textbf{(38)}$$

For laminar flow, as shown in equations (23) and (24), the Nusselt number is constant and, thus, the heat transfer rate is also constant as long as A_s/D_h is constant. Therefore, increasing or decreasing both the surface area and hydraulic diameter by the same factor does not affect the pressure, temperature and velocity of the gas inside the CFR if the flow is laminar. This is not true, however, for turbulent flows because the turbulence Nusselt number depends on the Reynolds number, which is a function of the hydraulic diameter.

For different porosity, the heat transfer rate is the same for fixed gas and wall temperature since both surface area and heat transfer coefficient are independent of porosity. However, the gas volume inside the CFR $V=AL=\phi A_D L$ is proportional to porosity. Therefore, the predicted pressure, temperature and velocity of the gas inside the CFR will be different for different values of porosity because, as shown in equation (6), what counts is the heat transfer rate per unit gas volume. This can also be easily understood from the energy equation

$$\dot{q}\Delta t = \rho V c_p (T_g^{\,n} - T_g^{\,n+1}) \quad \textbf{(39)}$$

or

$$T_g^{\,n+1} = T_g^{\,n} - \frac{\dot{q}\Delta t}{\rho V c_p} \quad \textbf{(40)}$$

where $\dot{q}>0$ is the amount of heat transfer rate from gas to solid. Therefore, for larger porosity, the gas volume inside the CFR is larger and the gas temperature at time step $n+1$ is higher if the gas temperature at time step n is the same.

RESULTS

The CFR models discussed above have been incorporated into SFLOW and the results of applying SFLOW to three sets of CFR tests, which simulate the RSRM nozzle-to-case joints and nozzle joint No. 2, are discussed in this section. The first two tests are cold flow tests and the flow through CFR is assumed to be adiabatic. The last test is a hot flow test and both pressure and temperature history at the joint inlet are specified in the SFLOW calculation.

Cold Flow Nozzle-to-Case Joint Test

Cold flow tests simulating the RSRM nozzle-to-case joint have been performed[5] where nitrogen (N_2) flows from a high-pressure tank though a CFR to the ambient conditions. SFLOW was applied to simulate these tests and the predicted tank pressure is compared with the measured data in this section. The 10% compression ratio case is shown first, followed by cases with compression ratios of 30%, 0% and −10%. For the 10% compression ratio case, the effects of permeability, Forschheimer constant, as well as porosity are discussed in detail.

By neglecting the transient term, convective term as well as the Forschheimer term in equation (26), the permeability can be derived from the measured pressure difference across the CFR, Δp, as

$$K = \frac{\mu L v}{\Delta p} \tag{41}$$

Assuming the gas temperature inside the tank $T=const$, the Darcy velocity in the above equation can be written as

$$v = \frac{(p_2 - p_1)V}{(t_2 - t_1)RT\rho A_D} \tag{42}$$

where V is the tank volume and p_1 and p_2 are the tank pressure at time t_1 and t_2, respectively. The permeability calculated using the above equations for the 10% compression ratio case is shown in Figure 1, which ranges from 4×10^{-11} in^2 to 1.2×10^{-10} in^2. (See ref. 27 for more details.) Although the permeability in Figure 1 varies with time, all SFLOW predictions shown in this paper assume a constant permeability (i.e., changes with neither time nor location).

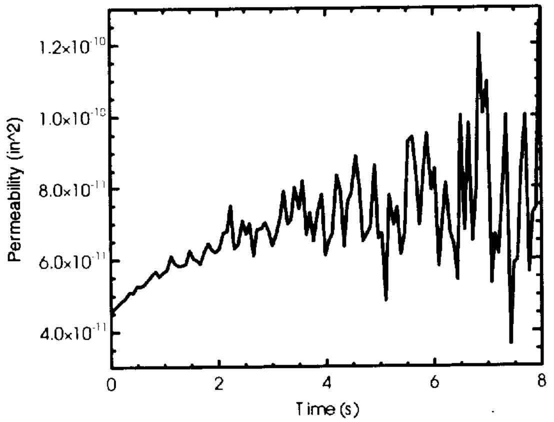

Figure 1: Permeability derived from the measured data for the 10% compression ratio case.

Figure 2 and Figure 3 show the comparison of predicted pressure with measured data for different values of permeability and Forschheimer constant, respectively. The porosity used is 0.01 and the friction factor is calculated from equation (32). Note that the effective porosity used here is much smaller than the measured value since a larger porosity corresponds to a larger friction factor, which requires smaller time step. As expected, the tank pressure drops faster for larger permeability and smaller Forschheimer constant due to the decrease in friction factor and increase in mass flow rate. It is also evident that the predicted pressure using a permeability of 8.5×10^{-11} in^2 and a Forschheimer constant of 0.632 agree very well with the measured data.

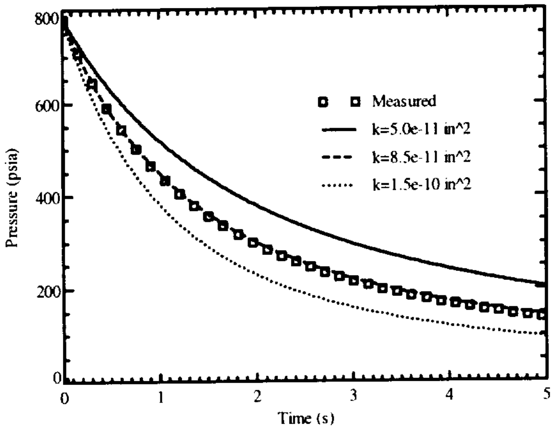

Figure 2: Comparison of predicted pressure and measured data for a porosity of 0.01 and c=0.632.

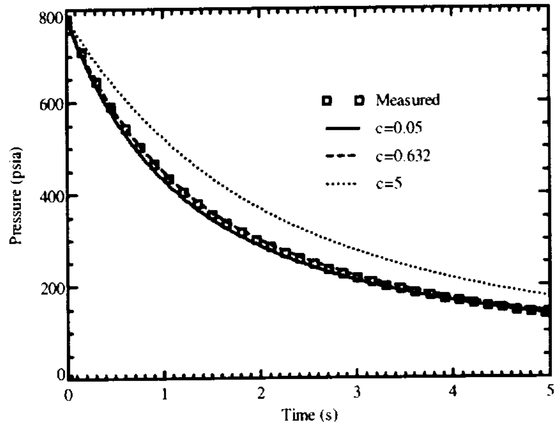

Figure 3: Comparison of predicted pressure and measured data for a porosity of 0.01 and permeability of 8.5×10^{-11} in^2.

Figure 4 shows the predicted tank pressure by assuming $c=0$ in equation (32). It is evident that, although the agreement is slightly better with a permeability of 8.0×10^{-11} in^2, the overall agreement is good with a permeability of 8.5×10^{-11} in^2, indicating that the effect of Forschheimer term is relatively small. Therefore, the Forschheimer term has been neglected in all results shown in the rest of this paper. Note also that these values of permeability are very close to that shown in Figure 1 derived from the measured data using equation (41).

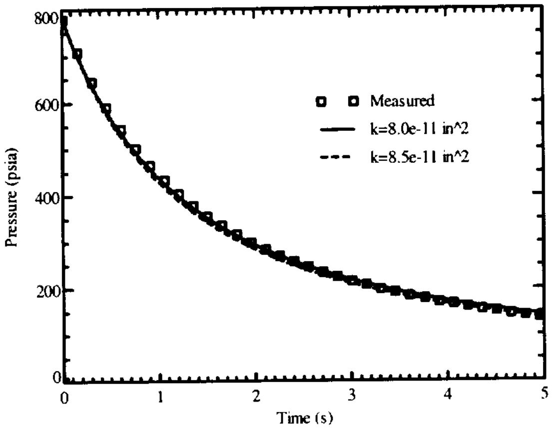

Figure 4: Comparison of predicted pressure and measured data for a porosity of 0.01 and c=0.

The mass flow rates at different downstream locations inside the CFR are shown in Figure 5. The mass flow rate at the beginning of the CFR is larger than that at the end, indicating that there is mass accumulation inside CFR and the flow is not steady. The mass flow rate also decreases with time due to the reduced pressure difference across the CFR as the tank used in the experiment drained.

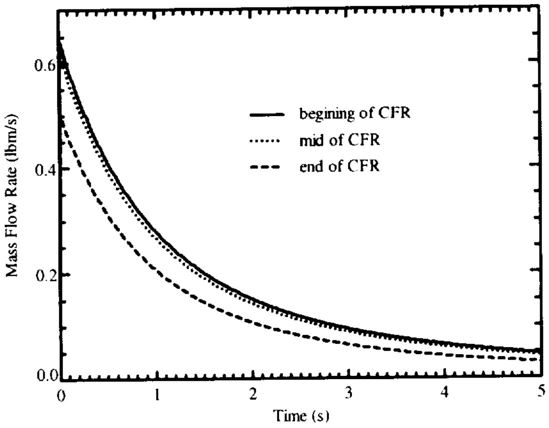

Figure 5: Predicted mass flow rate with a porosity of 0.01 and permeability of 8×10^{-11} in^2.

The Mach numbers at different downstream locations inside the CFR are shown in Figure 6. The flow for this case is not choked since the Mach number is smaller than unity at all times. The Mach number decreases with time due to the reduced mass flow rate shown in Figure 5 and increase with downstream location because of the friction.

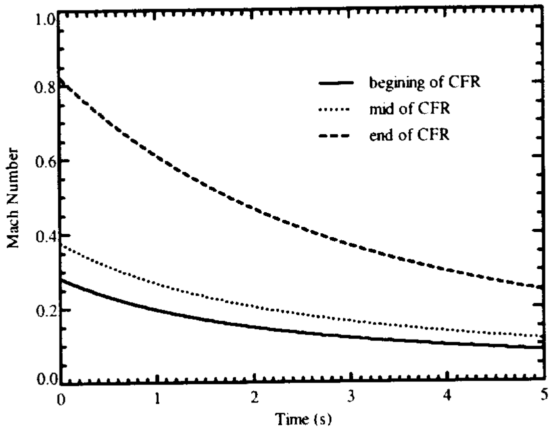

Figure 6: Predicted Mach number with a porosity of 0.01 and permeability of 8×10^{-11} in^2.

The friction factors at different downstream locations inside the CFR are shown in Figure 7. The friction factor increases with both time and downstream locations since, as shown in equation (35), the friction factor is inversely proportional to the mass flow rate. The friction factor ranges from 10 to more than 200, which is much larger than in a regular duct, due to the small permeability value.

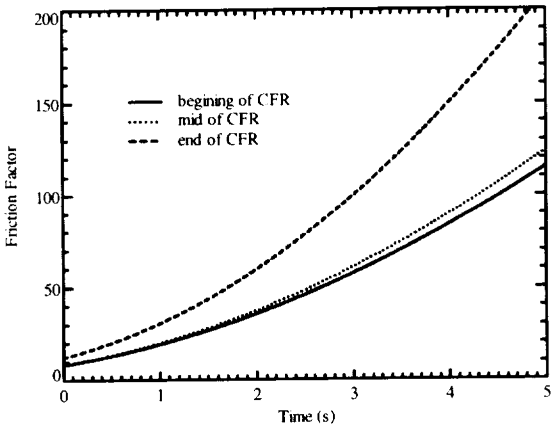

Figure 7: Predicted friction factor with a porosity of 0.01 and permeability of 8×10^{-11} in^2.

Figure 8 shows the Mach numbers at different downstream locations inside the CFR with a porosity of 0.002 and permeability of 8×10^{-11} in^2. The Mach number is much larger than that shown in Figure 6 with a porosity of 0.01 because the area is much smaller and velocity is larger. The flow across CFR is choked at all times and the Mach number at the end of the CFR is about unity. The oscillations of Mach number around unity occur because, as discussed in ref. 28, transonic flow is very sensitive to small changes. The magnitude of this oscillation can be reduced by using a smaller time step as shown in Figure 9, where a time step of 1×10^{-6} sec (instead of 1×10^{-5} sec) is applied.

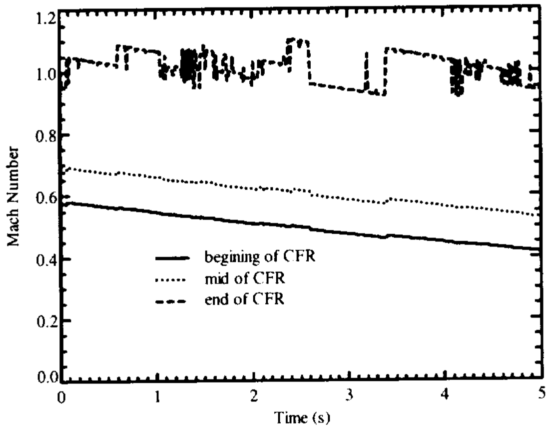

Figure 8: Predicted Mach number with a porosity of 0.002, permeability of 8×10^{-11} in^2, and time step of 1×10^{-5} sec.

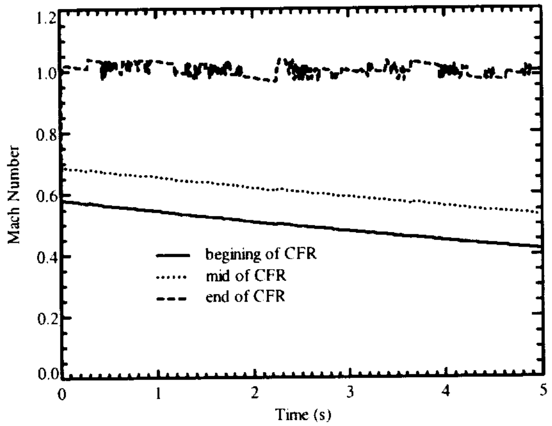

Figure 9: Predicted Mach number with a porosity of 0.002, permeability of 8×10^{-11} in^2, and time step of 1×10^{-6} sec.

The Mach numbers with a porosity of 0.005 and permeability of 8×10^{-11} in^2 are shown in Figure 10, where a time step of 1×10^{-6} sec is applied. The flow across CFR is choked for $t<0.5$ sec but unchoked after that time because of the reduced pressure difference across the CFR.

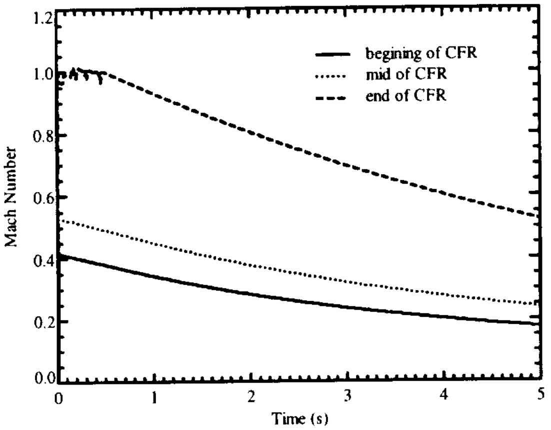

Figure 10: Predicted Mach number with a porosity of 0.005, permeability of 8×10^{-11} in^2, and time step of 1×10^{-6} sec.

The Mach numbers with a porosity of 0.02 and permeability of 8×10^{-11} in^2 are shown in Figure 11. The flow across CFR is not choked and the Mach number is much smaller than that using a porosity of 0.01.

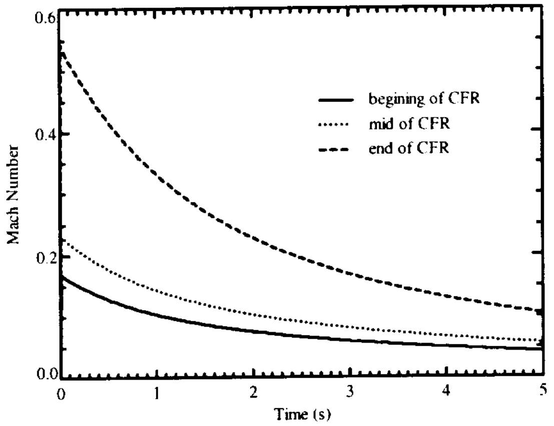

Figure 11: Predicted Mach number with a porosity of 0.02 and permeability of 8×10^{-11} in^2.

The effect of porosity on the predicted pressure is shown in Figure 12, where a permeability of 8.0×10^{-11} in^2 is applied. The tank pressure is the largest for ϕ=0.002 since, as discussed earlier, the flow is choked all the times. The pressure is smaller for ϕ=0.005 because the flow is choked only at $t<0.5$ sec while the pressure is even smaller for ϕ=0.01 and ϕ=0.02 due to the fact that the flow is never choked. The pressure for ϕ=0.01 and ϕ=0.02 are not exactly the same because of the transient and convective terms in equation (26).

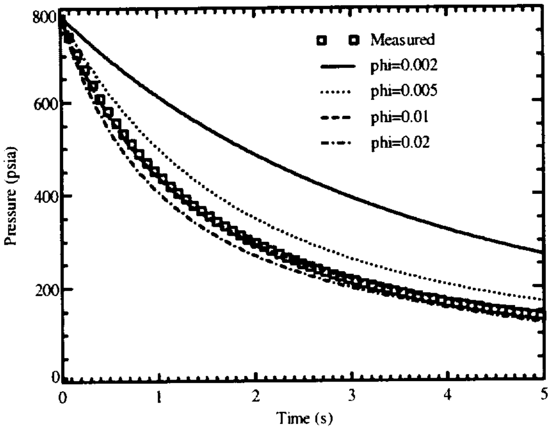

Figure 12: Comparison of predicted pressure and measured data for a permeability of 8x10^-11 in^2.

All the results shown above are for the 10% compression ratio case. The permeability calculated using equation (41) for other compression ratios is shown in Figure 13, which ranges from 3×10^{-11} in^2 to 2.5×10^{-10} in^2. The negative compression corresponds to an initial gap between the rope and the upper plate of the test fixture. It has been observed that blow-by does not occur for this small initial gap due to mechanical motion/deformation of the CFR into the open gap[5]. Note that the same Darcy area has been used for each different compression ratio. As expected, the permeability increases with decreasing compression ratio.

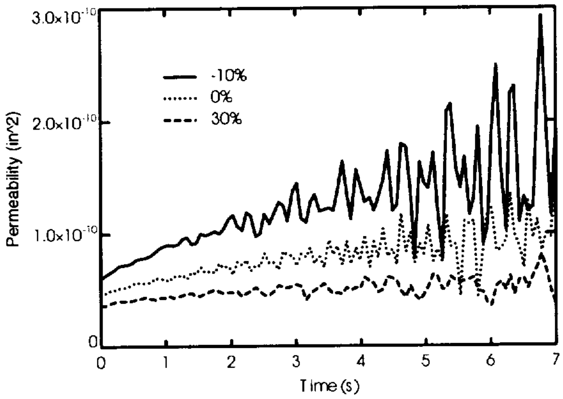

Figure 13: Permeability derived from the measured data for different compression ratios.

The predicted pressures for different compression ratios are compared with the measured data in Figure 14. A porosity of 0.01 is applied and the permeability used is $6\times10^{-11}in^2$, $9.2\times10^{-11}in^2$, and 1.5×10^{-10} in^2 for the 30%, 0%, and -10% compression ratios, respectively. These values of permeability are close to those shown in Figure 13 derived from the measured data using equation (41). The agreement of the predicted tank pressure with measured data is reasonable for all compression ratios.

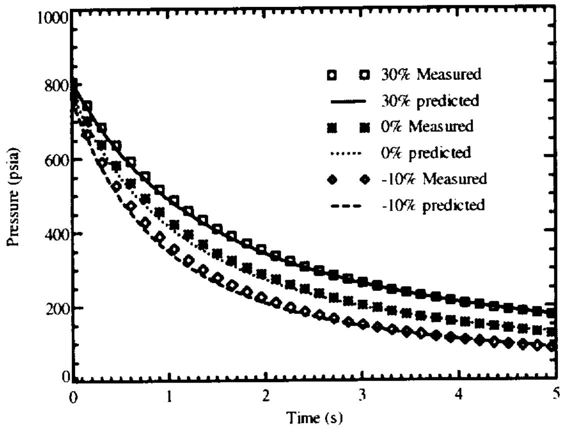

Figure 14: Comparison of predicted pressure and measured data for different compression ratios.

All the predictions shown above used the same Darcy area that was applied to reduce permeability even though the compression ratio is different. The predicted pressure for the 30% compression ratio case using the compressed frontal area as the Darcy area (i.e., the Darcy area is reduced by 30%) is shown in Figure 15, which indicates that, as discussed before, the permeability should be adjusted to $K=6\times10^{-11}in^2/0.7=8.57\times10^{-11}in^2$ in order to match the measured data. That is, the important parameter in SFLOW is the product of Darcy area and permeability whereas the flow solution is the same if the permeability is increased and the Darcy area is decreased by the same factor.

Cold Flow Joint 2 Test

Besides the cold flow nozzle-to-case joint test, additional testing was done using a fixture that modeled potential gland geometry for use in RSRM nozzle joint No. 2. SFLOW has been applied to simulate these tests and the results are shown below. The same parameters (e.g., Darcy area and porosity) as those in the nozzle-to-case joint discussed in the last section are used.

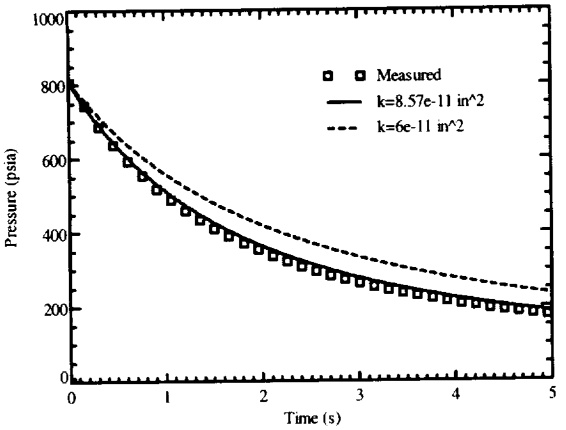

Figure 15: Comparison of predicted pressure and measured data using the adjusted area for the 30% compression ratio case.

The predicted pressures for different gap widths are compared with the measured data in Figure 16, which shows very good agreement for all gap widths. The permeability used is 4.4×10^{-11}in^2, 5.0×10^{-11}in^2, and 6.2×10^{-10} in^2 for the 0.04 in, 0.06 in, and 0.08 in gap widths, respectively. As expected, the permeability is larger for a larger gap width since the CFR is less compressed.

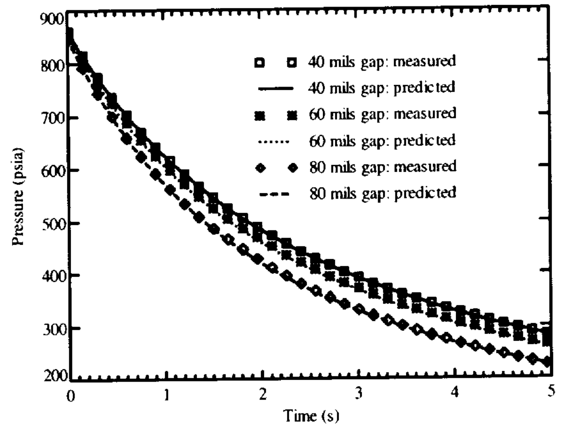

Figure 16: Comparison of predicted pressure and measured data for the RSRM Joint 2 test with different gap widths.

Hot Flow JES5 Test

The nozzle-to-case and joint 2 testing modeled above are cold flow tests, where the inlet gas temperature is very close to the ambient temperature. Therefore, the heat transfer between gas and solid walls is small and the process is assumed to be adiabatic in the SFLOW predictions. In the space shuttle RSRM, however, the combustion gas at the joint inlet is about 6000 R, which is much higher than the ambient temperature of about 540 R, and the heat transfer from this high-temperature gas to the solid surfaces should not be neglected. Therefore, hot flow tests called Joint Environment Simulator (JES)[6,24] have been carried out. SFLOW is applied to model these tests and some results from the JES5 modeling are discussed below.

The solid grid used in the SFLOW prediction is shown in Figure 17. The widths of the leak paths before and after the CFR are 0.065 in. In all results shown in this section, the Darcy area used in the SFLOW prediction is 0.065 in^2. From the results shown in last section, the permeability corresponding to a Darcy area of 7.96 in^2 for a gap width of 0.065 in is about 5.3×10^{-11} in^2. Therefore, the permeability used in the JES5 prediction should be $5.3\times10^{-11}\times7.96/0.065=6.5\times10^{-9}$ in^2. For all results shown in this section, except otherwise stated, the permeability, total surface area, and hydraulic diameter are 6.5×10^{-9} in^2, 0.2 in^2, and 9.3×10^{-3} in, respectively.

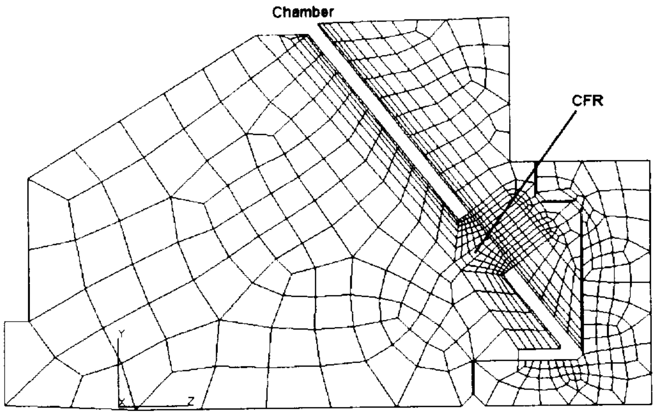

Figure 17: Solid grid used for the JES5 SFLOW prediction.

Figure 18 shows the predicted pressure using a porosity of 0.005, together with the measured pressure downstream of the CFR. The measured chamber pressure is used as the inlet stagnation pressure in the SFLOW prediction. The pressure before the CFR is identical to the chamber pressure because the CFR has much more resistance than the leak path. Although the fill time is very similar, the predicted pressure downstream of the CFR is smaller than the measured data at earlier times. Specifically, the predicted pressure shows a bigger pressure drop across the CFR than the measurement, which shows very small pressure lag when the chamber pressure rises very rapidly near 0.14 sec. It seems the predicted pressure makes more sense and the readings from the pressure transducer could be in error.

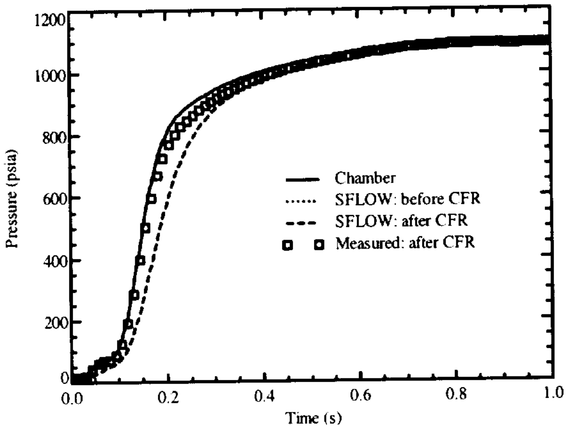

Figure 18: Comparison of predicted pressure using ϕ=0.005 with measured data.

The predicted temperatures at different downstream locations using a porosity of 0.005 are shown in Figure 19 and Figure 20. The temperature peaks at about 0.2 sec and then begins to decrease due to the decreased mass flow rate caused by the decreasing pressure difference across the CFR. The maximum temperature drops from 6000 R at the chamber to about 2400 R before the CFR. Inside the CFR, the gas temperature drops from 2400 R at the beginning to 1000 R at the mid and then to 700 R at the end, indicating that most of the temperature drop happens at the beginning of the CFR. At later times, the pressure drop across the CFR disappears, the flow through the CFR stops, and the gas temperature returns to ambient due to conduction.

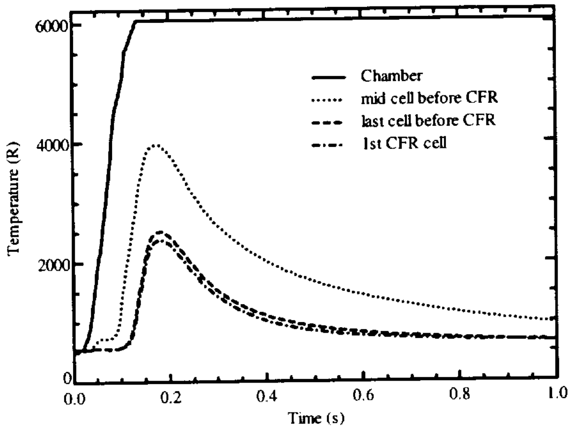

Figure 19: Predicted temperature before the CFR with ϕ=0.005.

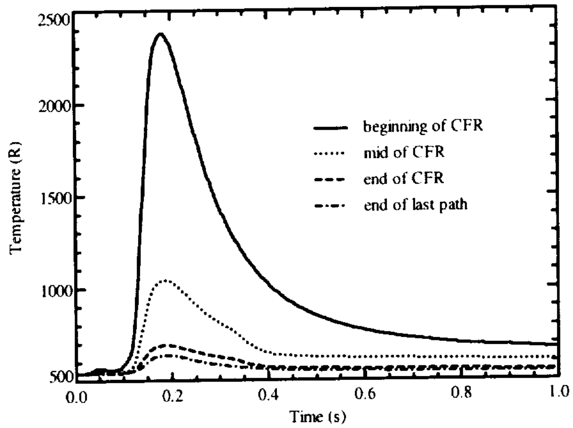

Figure 20: Predicted temperature inside and downstream of the CFR with ϕ=0.005.

Figure 21 and Figure 22 show the comparison of the SFLOW predicted temperature with the measured data right after the CFR and at the end of the last path after CFR, respectively. Also shown in the figures are the SFLOW predictions adjusted for the radiation heat transfer between the gas and solid walls as well as the conductive heat transfer inside the thermocouples. The adjusted SFLOW predictions agree well with the measured temperature before the peak temperature is reached but decreases faster than the measurement after that time. The lower predicted temperature suggested that the solid thermal conductivity used in the calculation is probably too high. The overall agreement is reasonable considering that the inlet temperature is

6000 R while the temperature downstream of the CFR is less than 700 R.

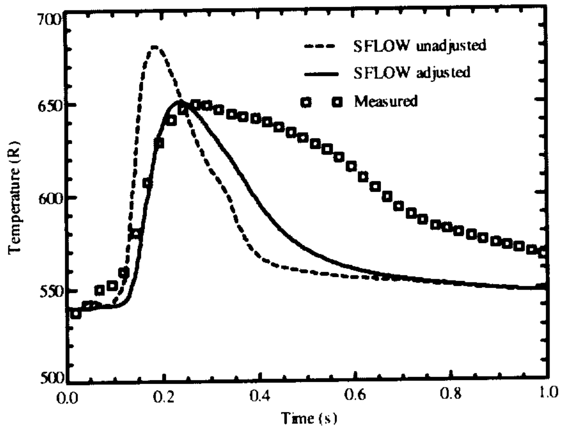

Figure 21: Comparison of predicted temperature using ϕ=0.005 with measured data right after the rope.

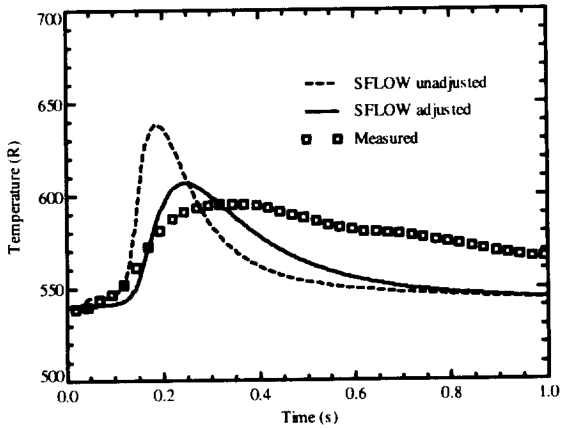

Figure 22: Comparison of predicted temperature using ϕ=0.005 with measured data at the end of last path.

The predicted difference between gas temperature and solid CFR temperature is shown in Figure 23. At 0.2 sec, the gas temperature is about 1750 R higher than the solid at the beginning of the CFR while the temperature difference is only about 150 R at the end of the CFR. At later times, the temperature difference is very small, indicating that the thermal equilibrium between gas and solid is reached.

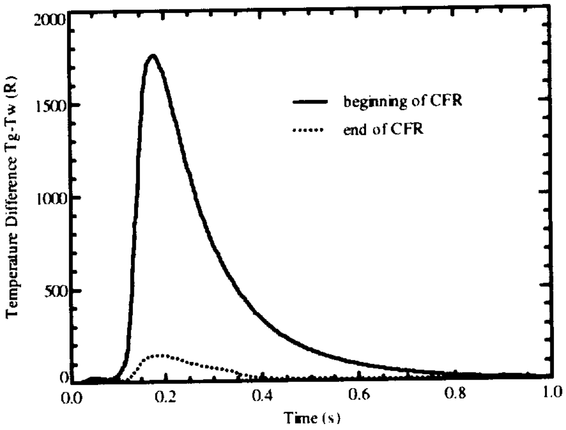

Figure 23: Predicted temperature difference (T_g-T_w) inside the CFR with ϕ=0.005.

Figure 24, Figure 25, and Figure 26 show the contours of the solid temperature at 0.33 sec, 0.66 sec and 1.0 sec, respectively. The solid temperature at the beginning of the CFR and near the leak path before the CFR is above 700 R while it is lower in other locations. At later times, more solid regions are heated up due to conduction.

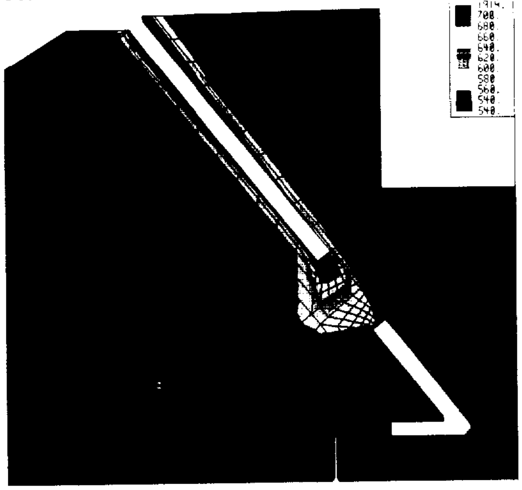

Figure 24: Isocontours of solid temperature at 0.33 sec with ϕ=0.005.

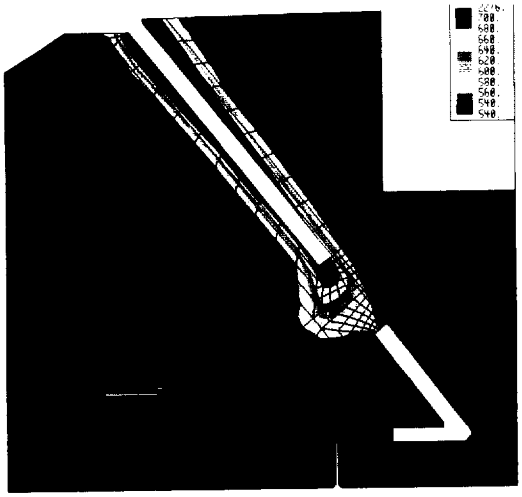

Figure 25: Isocontours of solid temperature at 0.66 sec with ϕ=0.005.

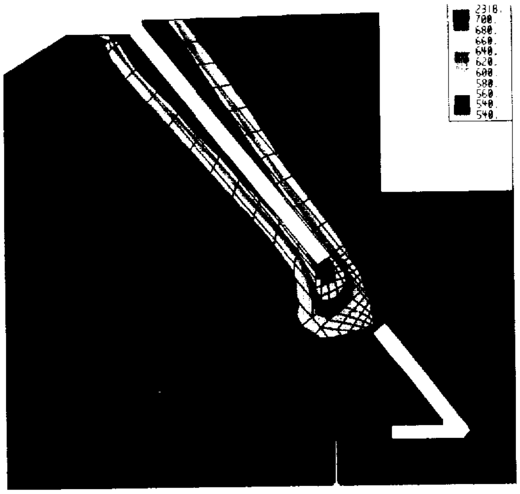

Figure 26: Isocontours of solid temperature at 1.0 sec with ϕ=0.005.

Figure 27 and Figure 28 show the predicted pressure and temperature using a porosity of 0.02, which is larger than the value of 0.005 used above. It is evident that the pressure downstream of the CFR is much larger than that shown in Figure 18. While the temperature at the beginning of the CFR is similar to the low porosity case shown in Figure 20, the temperatures at the mid and end of the CFR are much larger. This is because, as discussed earlier, the heat transfer rate per unit mass from gas to solid surfaces is much smaller for the large porosity case due to the increased gas volume inside the CFR.

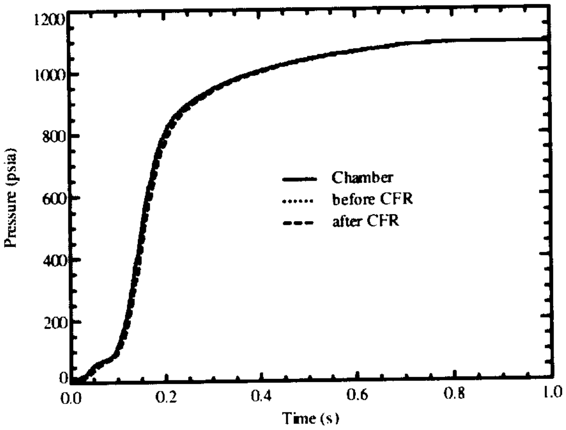

Figure 27: Predicted pressure using ϕ=0.02.

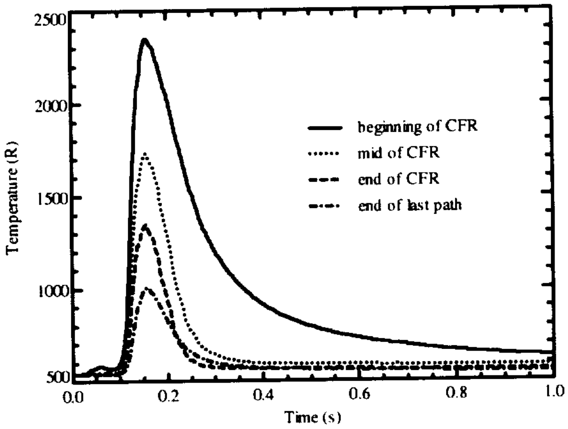

Figure 28: Predicted temperature using ϕ=0.02.

The predicted pressure and temperature by assuming there is no heat transfer between gas and solid everywhere are shown in Figure 29 and Figure 30, respectively. Similar to the large porosity case in Figure 27, the pressure downstream of the CFR is very close to the chamber pressure. The temperature is much larger than both the large and small porosity cases. In fact, the gas temperature inside the joint is even higher than the chamber temperature because of the adiabatic compression. For these conditions, the heat transfer from the hot combustion gas to the surrounding solid is the dominating driver for the problem. The adiabatic compression temperature for this case can be calculated as 6930 R, which is close to the SFLOW predicted gas temperature inside the CFR.

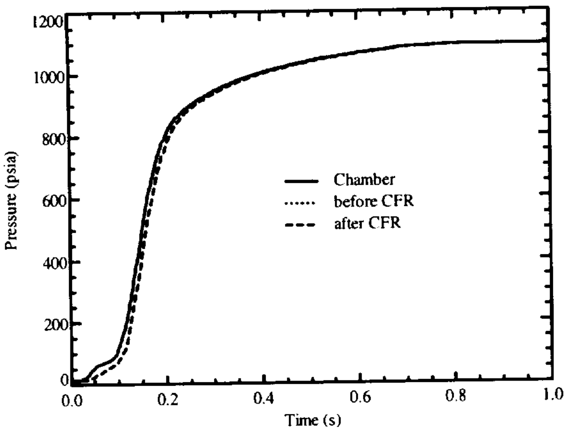

Figure 29: Predicted pressure using ϕ=0.005 and assuming no heat transfer.

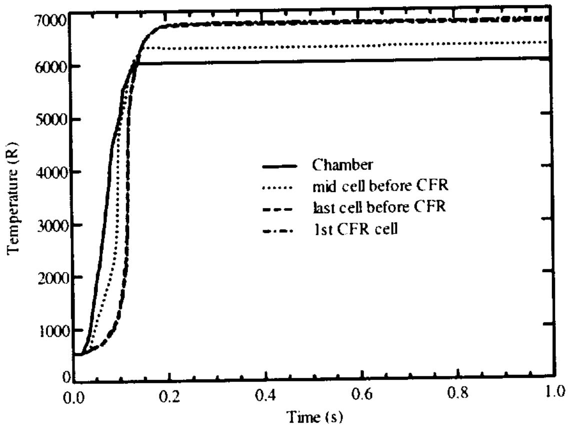

Figure 30: Predicted temperature using ϕ=0.005 and assuming no heat transfer.

Figure 31 and Figure 32 show the predicted pressure and temperature using a porosity of 0.005 and different permeability. The pressure and temperature change only slightly when the permeability is increased from 6×10^{-10} in^2 to 5×10^{-8} in^2 because, as discussed earlier, this problem is dominated by heat transfer and the effect of friction is small. The pressure downstream of the CFR increases with increasing permeability due to the smaller friction factor. While the temperature for $t<0.2$ sec is higher for larger permeability due to the larger mass flow rate, it is lower for $t>0.2$ sec because of the reduced pressure difference across the CFR.

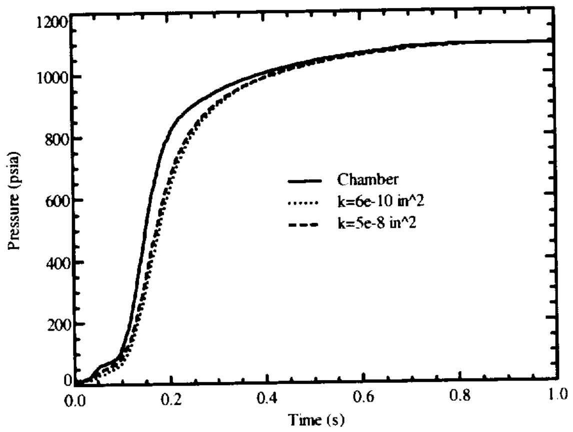

Figure 31: Predicted pressure using ϕ=0.005 and different permeability.

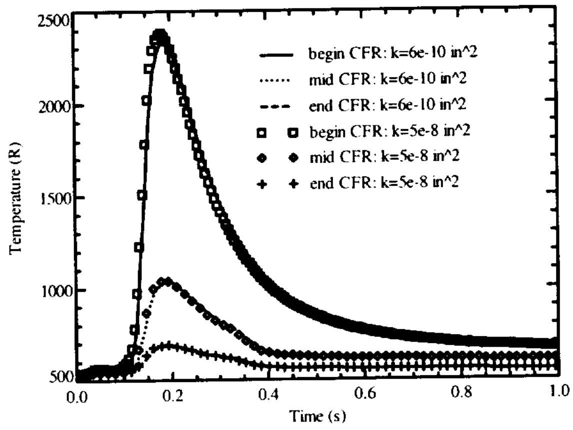

Figure 32: Predicted temperature using ϕ=0.005 and different permeability.

Figure 33 and Figure 34 show the predicted pressure and temperature using different values of hydraulic diameter and surface area. The pressure and temperature do not change when the surface area and hydraulic diameter are both decreased by a factor of 10 because, as discussed earlier, the ratio of surface area and hydraulic diameter is the same. The ratio of surface area with diameter used in Figure 33 and Figure 34 is A_s/D_h=21.5 in, which is the same as that used in Figure 18 and Figure 20. However, the pressure after the rope shown in Figure 18 is much smaller whereas the temperature inside the CFR shown in Figure 20 is much higher. This is because the Reynolds number is proportional to the hydraulic diameter and the large diameter used in Figure 18 and Figure 20 increases the Reynolds number to the turbulent region, which has much larger heat transfer coefficients than the laminar region. Figure 35 shows the Reynolds number Re=$\rho u D_h / \mu$ at the end of the CFR for different values of surface area and hydraulic diameter. The Reynolds number increases with increasing hydraulic diameter and the flow is turbulent between 0.1 sec and 0.3 sec for $D_h=9.3\times10^{-3}$ in while the flow is always laminar for $D_h=9.3\times10^{-4}$ in and $D_h=9.3\times10^{-5}$ in.

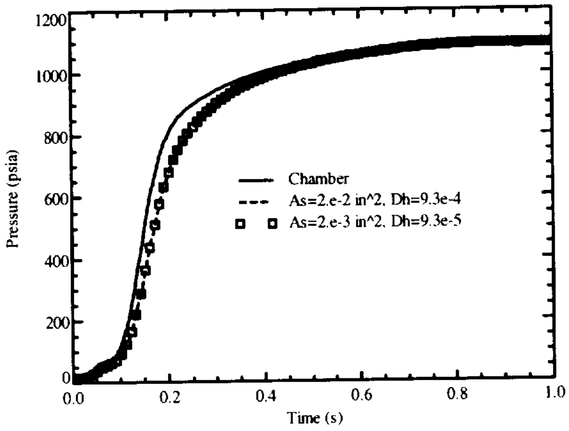

Figure 33: Predicted pressure using ϕ=0.005 and different surface area and hydraulic diameter.

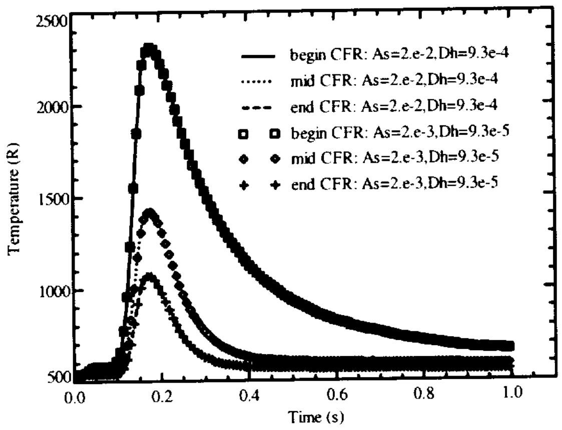

Figure 34: Predicted temperature using ϕ=0.005 and different surface area and hydraulic diameter.

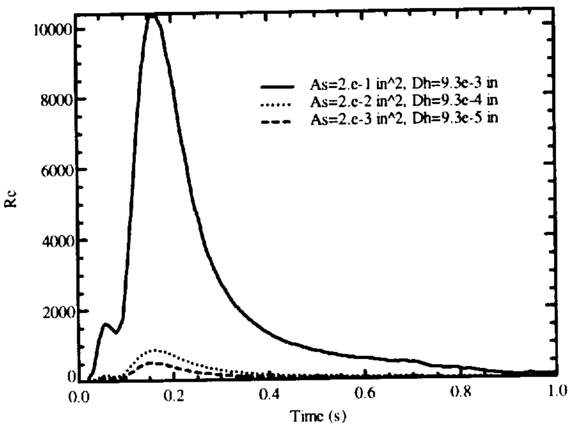

Figure 35: Predicted Reynolds number at the end of the CFR using ϕ=0.005.

CONCLUSIONS

Both flow and heat transfer models have been developed within the framework of SFLOW to predict the pressure, temperature and velocity of the gas inside the carbon fiber rope (CFR) for applications in the space shuttle reusable solid rocket motor joints. In particular, the CFR is modeled using an equivalent rectangular duct with a cross-section area, friction factor and heat transfer coefficient such that the mass flow rate, pressure drop, and heat transfer rate are the same as those in the CFR. The pressure, temperature and velocity of the gas inside this duct are calculated using the one-dimensional Navier-Stokes equations. Various subscale tests, both cold flow and hot flow, have been carried out to validate and refine the current CFR models. The predicted pressure and temperature history at various locations agree well with experimental measurements. The effect of Forschheimer term is relatively small. It was also found that the heat transfer from the hot combustion gas to the solid is the dominant driver in the applications of CFR to the space shuttle rocket joints.

The input parameters of the CFR model are Darcy area, hydraulic diameter, permeability, Forschheimer constant, total surface area, and porosity, all of which are independent of both location and time. The effects of these parameters have been studied in detail and the results are summarized below

- A large permeability corresponds to small friction factor and, thus, large mass flow rate and small pressure drop across the CFR.
- A small Forschheimer constant has the same effect as a large permeability.

- If the flow is adiabatic, reducing the Darcy area and increasing the permeability by the same factor do not affect the mass flow rate and pressure drop.
- If the process is adiabatic, the hydraulic diameter has no effect on the mass flow rate although the friction factor is linearly proportional to the hydraulic diameter.
- If the flow across the CFR is not choked and there is no heat transfer, the porosity has no effect on the solution of gas flow through a CFR when the transient and convective terms are neglected.
- If the flow is choked and adiabatic, increasing the porosity will increase the mass flow rate even though the friction factor is also increased.
- If there is heat transfer between gas and solid, the porosity affects the amount of gas inside the CFR and, thus, affects the flow solution.
- If the flow is laminar, increasing or decreasing both the surface area and hydraulic diameter by the same factor does not affect the pressure, temperature and velocity of the gas inside the CFR.

Some shortcomings of this CFR model are that the total surface area needs to be specified and the heat transfer coefficient is obtained from pipe correlations. Testing is underway to measure the product of heat transfer coefficient and surface area as a function of geometry, Reynolds number, and Prandtl number. Results from this testing will be used to develop a new heat transfer model where the surface area is not needed and the pipe correlations are not used. This new model will be incorporated into SFLOW and validated against test data.

REFERENCE

1. Steinetz, B.M., Melis, M.E., Orletske, D. and Test, M.G. 1991 "High temperature NASP engine seal development," *NASA TM*-103716.
2. Steinetz, B.M., Adams, M.L., Bartolotta, P.A., Darolia, R., and Olsen, A. 1997 "High temperature braided rope seals for static sealing applications," *Journal of Propulsion and Power*, Vol. 13, pp. 675-682.
3. Totman, P., Prince, A.S., Frost, D. and Himebaugh, P. 1999 "Alternatives to silicon rubber thermal barrier in RSRM nozzle joints," *AIAA Paper* 99-2796.
4. Steinetz, B.M. and Dunlap, P.H. 1999 "Development of thermal barriers for solid rocket motor nozzle joints," *AIAA Paper* 99-2823.
5. Ewing, M.E., McGuire, J.R., McWhorter, B.B. and Frost, D.L. 1999 "Performance enhancement of the space shuttle RSRM nozzle-to-case joint using a carbon rope barrier," *AIAA paper* 99-2899.
6. Bauer, P. 2000 "Development of an enhanced thermal barrier for RSRM nozzle joints," *AIAA paper* 2000-3566.
7. Steinetz, B.M. and Dunlap, P.H. 1998 "Feasibility assessment of thermal barrier seals for extreme transient temperatures," *AIAA paper* 98-3288.
8. Foote, J.O. 1997 "Titan IV solid rocket motor upgrade program at Alliant Techsystems, Inc.," *AIAA Paper* 97-2991.
9. Wang, Q., Mathias, E.C., Heman, J.R. and Smith, C.W. 2000 "A thermal-flow code for modeling gas dynamics and heat transfer in space shuttle solid rocket motor joints," *AIAA paper* 2000-3189.
10. Network Analysis Inc., 1996 *SINDA/G User's Guide*, Tempe, AZ.
11. Golafshani, M. and Loh, H.T. 1989 "Computation of two-phase viscous flow in solid rocket motors using a flux-split Eulerian-Lagrangian technique," *AIAA Paper* 89-2785.
12. Loh, H.T., Smith-Kent, R., Perkins, F. and Chwalowski, P. 1996 "Evaluation of aft skirt length effects on rocket motor base heat using computational fluid dynamics," *AIAA paper* 96-2645.
13. Wang, Q. 1999 "User's guide for SHARP: a general CFD solver," *Thiokol Corporation TR*-11582.
14. Clayton, J.L. 1995 "Joint pressurization routine (JPR) theoretical development and users manual," *NASA-MSFC Internal Memorandum* ED66 (95-01).
15. O'Malley, M. 1988 "A model for predicting RSRM joint volume pressurization, temperature transients, and ablation," *AIAA Paper* 88-3332.
16. Mutharasan, R.M., Steinetz, B.M., Tao, X.M., and Ko, F. 1991 "Development of braided rope seals for hypersonic engine applications: Part II: flow modeling," *AIAA Paper* 91-2495.
17. Mutharasan, R.M., Steinetz, B.M., Tao, X.M., and Ko, F. 1993 "Development of braided rope seals for hypersonic engine applications: flow modeling," *Journal of Propulsion and Power*, Vol. 9, pp. 456-461.
18. Cai, Z., Mutharasan, R., Ko, F.K. and Steinetz, B.M. 1993 "Development of hypersonic

engine seals: flow effects of preload and engine pressures," *AIAA paper* 93-1998.

19. Cai, Z., Mutharasan, R., Ko, F.K. and Steinetz, B.M. 1994 "Development of hypersonic engine seals: flow effects of preload and engine pressures," *Journal of Propulsion and Power*, Vol. 10, pp. 884-889.
20. Emanuel, G. and Jones, J.P. 1968 "Compressible flow through a porous plate," *Int. J. Heat Mass Transfer*, Vol. 11, pp. 827-836.
21. Beavers, G.S. and Sparrow, E.M. 1971 "Compressible gas flow through a porous materical," *Int. J. Heat Mass Transfer*, Vol. 14, pp. 1855-1859.
22. Kaviany, M. 1995 *Principles of Heat Transfer in Porous Media*, Springer-Verlag, New York.
23. Nield, D.A. and Bejan, A. 1992 *Convection in Porous Media*, Springer-Verlag, New York.
24. Clayton, J.L. 2001 "Thermal analysis of a carbon fiber rope barrier for use in the reusable solid rocket motor nozzle joint-2," presented at the *21st Rocket Nozzle Technology Subcommittee Meeting*, 26-30 March 2001,Cocoa Beach, FL.
25. Idelchik, I.E. 1986 *Handbook of Hydraulic Resistance*, 2nd Edition, Hemisphere Publishing Corp.
26. Bellettre, J., Bataille, F., Rodet, J.C. and Lallemand, A. 2000 "Thermal behavior of porous plates subjected to air blowing," *Journal of Thermophysics and Heat Transfer*, Vol. 14, pp. 523-532.
27. Ewing, M. 2000 "Carbon fiber rope: preliminary flow characterization and modeling approaches," *Thiokol Corporation TWR*-77047.
28. Anderson, J.D. 1990 *Modern Compressible Flow: With Historical Perspective*, 2nd edition, McGraw-Hill Publishing Company.